Segmentation-Driven Image Fusion Based on Alpha-Stable Modeling of Wavelet Coefficients

Tao Wan, *Student Member, IEEE*, Nishan Canagarajah, *Member, IEEE*, and Alin Achim, *Senior Member, IEEE*

***Abstract*—A novel region-based image fusion framework based on multiscale image segmentation and statistical feature extraction is proposed. A dual-tree complex wavelet transform (DT-CWT) and a statistical region merging algorithm are used to produce a region map of the source images. The input images are partitioned into meaningful regions containing salient information via symmetric alpha-stable ($S\alpha S$) distributions. The region features are then modeled using bivariate alpha-stable ($B\alpha S$) distributions, and the statistical measure of similarity between corresponding regions of the source images is calculated as the Kullback–Leibler distance (KLD) between the estimated $B\alpha S$ models. Finally, a segmentation-driven approach is used to fuse the images, region by region, in the complex wavelet domain. A novel decision method is introduced by considering the local statistical properties within the regions, which significantly improves the reliability of the feature selection and fusion processes. Simulation results demonstrate that the bivariate alpha-stable model outperforms the univariate alpha-stable and generalized Gaussian densities by not only capturing the heavy-tailed behavior of the subband marginal distribution, but also the strong statistical dependencies between wavelet coefficients at different scales. The experiments show that our algorithm achieves better performance in comparison with previously proposed pixel and region-level fusion approaches in both subjective and objective evaluation tests.**

***Index Terms*—Bivariate alpha-stable distributions, image segmentation, Kullback–Leibler distance, region-based image fusion, wavelet decomposition.**

I. Introduction

MULTISENSOR image fusion provides a mechanism to combine multiple images into a single representation that has the potential to aid human visual perception or subsequent image processing tasks. Such algorithms endeavor to create a fused image containing the salient information from each source image without introducing artefacts or inconsistencies. The fusion process can be performed at four main levels [1]: signal, pixel, feature and semantic. In past decades, many pixel-level fusion schemes have been proposed. These range from simple averaging of the pixel values of registered images to more complex multiresolution (MR) pyramids and wavelet methods. For example in [2], an image fusion method was proposed using a wavelet transform and a window-based maximum selection rule. Achim *et al.* derived a fusion approach using fractional lower order moments as a fusion rule at the pixel level [3]. The majority of applications of a fusion scheme attempt to process features within the image. One way of achieving feature-level fusion is by employing a region-based approach. Compared with pixel-level image fusion, region-based fusion schemes have a number of perceived advantages, including reduced sensitivity to noise, features enhancement and increased flexibility in choosing intelligent fusion rules. In [4], Piella presented a multiresolution image fusion algorithm guided by a multimodal segmentation. Lewis *et al.* [5] also proposed a region-level fusion method in conjunction with a combined morphological-spectral unsupervised image segmentation [6]. These methods first transform the source images to multiresolution representations, and regions are extracted from the transform coefficients in each scale. Some simple activity level measurements are calculated within each region. The source images are then fused based on these activity level measurements using inverse MR transform. This process is shown in Fig. 1 for the case of two input source images. A sophisticated image fusion method based on a statistical signal processing approach has been proposed in [7], in which a Gaussian mixture distortion model was built and used to produce the fused image. The model parameters are estimated using the iterative expectation-maximization algorithm that is computationally complex. All these methods fail to take into account the significance of the statistical characteristics of regions, which can be used to improve the accuracy of the decision procedure in image fusion applications.

The quality of the image segmentation is of vital importance to the region-based fusion process. For the correct features to be present in the fused image, the segmentation should ideally detect all the salient objects in the input images. Moreover, all required features should be segmented as single separate regions. If a feature is split into more than one region, each will be treated separately, possibly introducing artefacts into the fused image. If a feature is missed, it will not be incorporated in the fused image. The segmentation algorithm also should be able to provide precise region boundaries which can help to eliminate blocking and blurring effects in the fused image. State-of-the-art segmentation methods include stochastic model-based approaches [8]–[10], morphological watershed-based region growing [6], JSEG [11], normalized cuts [12], and perceptual partitioning [13].

In recent work, we have showed that successful statistical image processing algorithms can be developed if they take into consideration the actual heavy-tailed behaviour of most real life signals [14], [15]. Specifically, we have shown that

Manuscript received February 14, 2008; revised February 09, 2009. First published April 28, 2009; current version published May 15, 2009. The work of T. Wan was supported by an Overseas Research Students Award (ORSAS). The associate editor coordinating the review of this manuscript and approving it for publication was Dr. Alex C. Kot.

The authors are with the Centre for Communications Research, Department of Electrical and Electronic Engineering, University of Bristol, Bristol BS8 1UB, U.K. (e-mail: Tao.Wan@bristol.ac.uk; Nishan.Canagarajah@bristol.ac.uk; Alin.Achim@bristol.ac.uk).

Color versions of one or more of the figures in this paper are available online at http://ieeexplore.ieee.org.

Digital Object Identifier 10.1109/TMM.2009.2017640

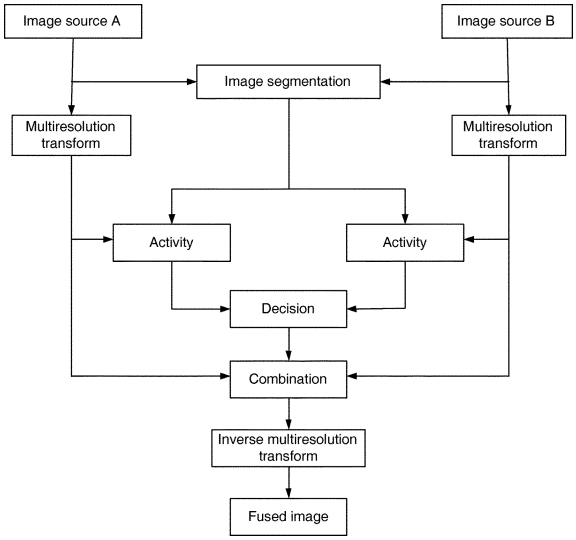

Fig. 1. Generic region-based multiresolution image fusion scheme.

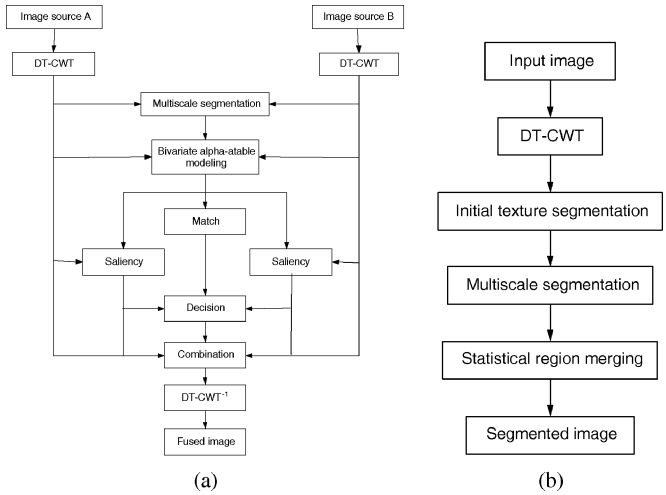

Fig. 2. Proposed region-based image fusion framework. (a) Region-based fusion scheme using $\mathrm{B}\alpha\mathrm{S}$ model. (b) Multiscale image segmentation algorithm.

wavelet decomposition coefficients of images are best modeled by symmetric alpha-stable distributions [16], [17], a family of heavy-tailed densities. Hence, we propose a novel statistical image segmentation and region-based fusion framework using an alpha-stable modeling of regions for optimal segmentation and fusion results. While having low complexity, the majority of fusion methods employing the marginal distributions ignore the correlations between wavelet coefficients, especially the correlations across the wavelet decomposition scales. There is an inter-scale dependency, most notable between a wavelet coefficient at a coarse level and the four coefficients at the previous adjacent level that correspond to the same location in the image.

In this paper, we address these problems by using a bivariate alpha-stable model to characterize the local region features and capture both wavelet subband marginal distributions and inter-scale dependencies of wavelet transform coefficients. Fig. 2(a) illustrates the block diagram of the proposed region-based image fusion scheme. First, the multisensor images are decomposed into multiresolution representations using the dual-tree complex wavelet transform [18], which provides near shift invariance and good directional selectivity compared to the standard wavelet transform. The source images are partitioned into relatively homogeneous regions by applying an adaptive version of the multiscale image segmentation presented in our previous work [19], [20]. The block diagram of the algorithm is shown in Fig. 2(b). The input region maps are integrated into a joint region map using an union operation. A $\mathrm{B}\alpha\mathrm{S}$ model is then built to characterize each region properties, which results in a good modeling of both the non-Gaussian heavy-tailed distributions and the property of persistence across scales in a wavelet decomposition. The Kullback–Leibler distance of the same regions is computed as similarity measure between the input images, and the $\mathrm{B}\alpha\mathrm{S}$ model parameters are used to measure the amount of salient information contained in the regions. Then, decision map based on the match and saliency measures is produced to combine the detail coefficients of the MR decompositions of the various sources by considering the local statistical features of the regions modeled via $\mathrm{B}\alpha\mathrm{S}$ distributions. Finally, the approximation coefficients of the highest decomposition level from the input images are combined by a weighted average method using region information entropy. The key to the success of the proposed algorithm is that the statistical modeling techniques and the region feature extraction are integrated into a single image fusion framework to achieve reliable and superior fusion performance.

The innovative aspects of the present work consist of the following: First, this work extends our recent research work on image segmentation [19], [20] to deal with multimodal images. The segmentation algorithm combined with a fusion process forms a statistical image fusion framework to perform precise and effective image segmentation and fusion. Second, a new region-based image fusion strategy is proposed that incorporates the local statistical characteristics of regions, leading to a better decision process and a robust fusion scheme. Third, the use of stable models as the basis for the presented methodology leads to superior overall performance in comparison with the generalized Gaussian distribution (GGD) [21]. Finally, the methodology presented in this paper can be seen as a general framework for segmentation-driven image fusion. This framework has the potential to be adapted for eventual use with different statistical models, as appropriate for particular applications.

The structure of the paper is as follows: In Section II, the image segmentation component of our algorithm is introduced. Section III describes the wavelet-domain image fusion algorithm, which is based on the bivariate alpha-stable model. Fusion results, using both subjective tests and objective performance measurements, are presented in Section IV. Finally, conclusions and future work are summarized in Section V.

II. Image Segmentation Algorithm

In this section, we describe a multiscale[1] image segmentation algorithm in which the texture features are modeled by symmetric alpha-stable distributions. As shown in Fig. 2(b),

[1]Multiscale in this context refers to applying various window size to the image in order to capture the colour and texture features.

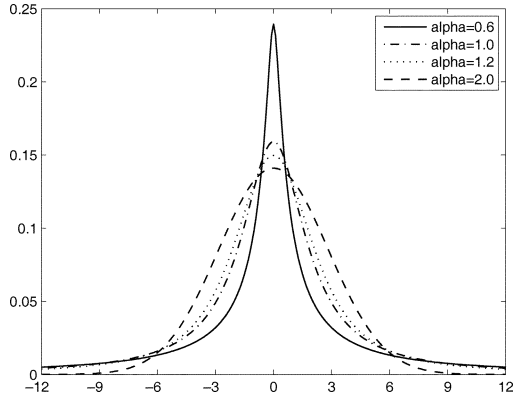

Fig. 3. Graphs of symmetric alpha-stable densities corresponding to the values $\alpha = 0.6$, $\alpha = 1.0$, $\alpha = 1.2$, and $\alpha = 2.0$. For all the graphs, $\gamma = 2.0$.

the algorithm comprises three components. First, the input image is roughly segmented into textured and nontextured regions using the dual-tree complex wavelet transform with the subband coefficients modeled as SαS random variables. A multiscale segmentation is then applied to the resulting regions, according to the local texture characteristics. Finally, a statistical region merging approach is developed by measuring the Kullback–Leibler distance between estimated SαS models for the adjacent segments. A preliminary version of this methodology has been already reported in [20]. The main advantage of the method presented here is that it can handle multimodal images.

A. Univariate Symmetric Alpha-Stable Distributions

This subsection is intended to provide a brief introduction on the symmetric alpha-stable model used to characterize the wavelet subband coefficients of multisensor images in the initial texture segmentation and region merging stages. The appeal of SαS distributions as a statistical model for signals derives from the stability property and the generalized central limit theorem [17]. Due to lack of a compact analytical expression for their probability density function (pdf), the SαS distributions are best defined by their characteristic functions as follows:

$$\varphi(\omega) = \exp(j\delta\omega - \gamma|\omega|^{\alpha}) \tag{1}$$

where α ($0 < \alpha \leq 2$) is the characteristic exponent, δ ($-\infty < \delta < \infty$) is the location parameter, and γ ($\gamma > 0$) is the dispersion of the distribution. For values of α in the interval (1, 2], the location parameter δ corresponds to the mean of the SαS distribution, while for $0 < \alpha \leq 1$, δ corresponds to its median. The dispersion parameter γ determines the spread of the distribution around its location parameter δ, similar to the variance of the Gaussian distribution. Gaussian processes are stable processes with $\alpha = 2$ while Cauchy processes result when $\alpha = 1$.

The characteristic exponent α is the most important parameter of the SαS distribution and it determines the shape of the distribution. Fig. 3 shows the SαS density functions with a few values of the characteristic exponent α. The smaller the characteristic exponent is, the heavier the tails of the SαS density. This implies that random variables following SαS distributions with small characteristic exponents are highly impulsive. In the following subsection, we show how α can be used as a texture descriptor in the texture segmentation algorithm.

B. Initial Texture Segmentation Using DT-CWT and SαS

Statistical modeling is much easier to perform in a suitable transform space where simple models with a small number of parameters can describe the data, rather than on the original image pixel values. Wavelets have emerged as an effective tool to analyze texture information as they provide a natural partitioning of the image spectrum into multiscale and oriented subbands. In this work, we use a three-scale DT-CWT [18] with six orientations, which is able to provide approximate shift invariance and directional selectivity while preserving the usual properties of perfect reconstruction and computational efficiency. The marginal distribution of the subband coefficients is well captured by adaptively estimating the two parameters α and γ of SαS distributions, which are defined in (1). Here, we assume that the location parameter $\delta = 0$ in the complex wavelet domain. Parameters α and γ can be obtained through log absolute moment of the wavelet coefficients [22]. In our work, the above estimation is implemented in a square-shaped neighborhood of size 7×7 around each reference coefficient as follows:

$$X = [w_i(x,y)] \quad i = 1,2,3,\ldots,18 \quad (x,y) \in W \tag{2}$$

$$Y = \log|X| \tag{3}$$

where W refers to the 7×7 window, and $w_i(x,y)$ is the detail coefficient in the i^{th} subband at location (x,y). It can be shown [22] that the mean and variance of Y are, respectively, given by

$$E(Y) = \frac{\alpha - 1}{\alpha} C_e + \frac{\log(\gamma)}{\alpha} \tag{4}$$

where $C_e = 0.5772166\ldots$ is the Euler constant, and

$$E([Y - E(Y)]^2) = \frac{\pi^2}{12}\frac{\alpha^2 + 2}{\alpha^2}. \tag{5}$$

The estimation process simply involves solving (5) for α and substituting back in (4) to find the value of the dispersion parameter γ. Therefore, the feature value $T(x,y)$ at the pixel location (x,y) is defined as

$$T(x,y) = \{\alpha_i(x,y), \gamma_i(x,y)\} \quad i = 1,2,3,\ldots,18 \tag{6}$$

where i is the index of the ith subband.

In order to obtain a uniform characterization of texture, median filtering [23] is employed on $T(x,y)$ within each subband to filter out the texture associated with transitions between regions. Finally, a two-level K-means algorithm is used to assign the pixels to textured and nontextured regions. A pixel is then classified as textured if the proportion of the number of the subbands belonging to the textured region is above a threshold P. Our experiments show that $P = 0.7$ is a good choice for thresholding multisensor images. Compared with [19], the threshold can be adjusted to the type of image. This property is useful for the segmentation algorithm which can handle not only natural images, but also images obtained using other modalities. In Fig. 4, we compare the performance of the proposed approach with that of simpler methods that only use DT-CWT or Gabor coefficients as in [19]. From the figure it can be seen that the new approach provides better texture segmentation with a compact grouping.

C. Multiscale Image Segmentation

The textured and nontextured regions are further segmented into relatively small and homogeneous regions while retaining the boundaries between adjacent regions. The dominant

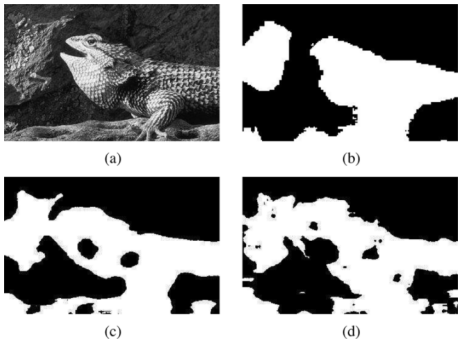

Fig. 4. Texture segmentation. (a) Original image. (b) Texture map using $\mathrm{S}\alpha\mathrm{S}$ model. (c) Texture map using DT-CWT coefficients. (d) Texture map using Gabor decomposition coefficients. White regions correspond to textured regions, and black regions correspond to nontextured regions.

greylevels are first extracted based on peer group filtering (PGF) [24] and the generalized Lloyd algorithm [25]. Then, the JSEG algorithm proposed by Deng *et al.* in [11] is used to minimize the cost associated with partitioning an image at different scales. A bigger window size is used for high scales, which are useful for detecting texture boundaries, while lower scales are employed in order to localize the intensity of greyscale edges. It is reasonable to apply lower scales to nontextured regions, which contain relatively homogeneous texture, while higher scales are adopted for the textured regions to capture the texture boundaries. In contrast with JSEG, which does not account for the local texture difference between the image regions, the strength of this approach is that we are able to apply the multiscale segmentation simultaneously to the same image according to the local texture characteristics.

However, the resulting boundary locations between textured and nontextured regions are not the actual boundaries due to the fact that K-means clustering can only segment the image into rough regions. Moreover, multiscale segmentation provides accurate results only within the textured and nontextured regions. Consequently, a boundary refinement step is needed in order to adjust the boundaries between the two regions. A pixel is assigned to the neighbor class that has the minimum D value using the following function:

$$D = Dist(C^0, C^j) + a(S_4^j - D_4^j) + b(S_8^j - D_8^j) \quad (7)$$

where $Dist$ refers to the Euclidean distance measure, C^0 and C^j are the dominant greylevels vectors of the current pixel and its jth neighbor segment, S_4^j and S_8^j are the numbers of 4- and 8-neighbor pixels belonging to the jth segment, while D_4^j and D_8^j are the numbers of 4- and 8-neighbor pixels belonging to the different classes of the jth segment. a and b represent the strength of the spatial constraint. Specifically, as a and b increase, a pixel is more likely to belong to the class to which many of its neighbors also belong. Thus region boundary smoothness is achieved.

D. Statistical Region Merging

In general, the result of applying the algorithm described in the previous subsections leads to over-segmentation. A statistical region merging method is implemented by using $\mathrm{S}\alpha\mathrm{S}$ distributions to appropriately model wavelet coefficients within the segmented regions. In this work, the regions are classified into two categories. The segments with more than a given threshold percentage of their pixels belonging to the nontextured areas are categorized as nontextured segments, and the remaining segments are classified as textured segments. Accordingly, segmented regions are considered individually rather than globally.

A corresponding merging criterion is provided for each category. The difference lies in the way the features are extracted within the regions. Nontextured segments are merged based on their greyscale intensity similarity. To achieve this, the Euclidean distance of the greylevel histograms extracted from the neighboring nontextured segments is calculated. For textured segments, region similarity is measured using statistical model parameters followed by computing the Kullback–Leibler distance.

In [26], the authors introduced a statistical framework for texture image retrieval where the marginal density of coefficients is approximated by symmetric alpha-stable distributions, and texture similarity is measured by means of the Kullback–Leibler distance between model parameters. Motivated by their work, we model subband complex wavelet coefficients in the textured regions independently using $\mathrm{S}\alpha\mathrm{S}$ densities, where model parameters can be estimated through the method proposed in [22]. Comparing with the parameter estimator described in the previous subsection on the initial texture segmentation, which lacks *a priori* knowledge about the image, here we accelerate the estimation process by incorporating the region information instead of using a window mask for each image pixel. Therefore, the characteristics of the region can be completely defined via two parameters α and γ. There is no closed-form expression for the KLD between two general $\mathrm{S}\alpha\mathrm{S}$ distributions, which are neither Cauchy nor Gaussian. By applying the KLD on a normalized version of the $\mathrm{S}\alpha\mathrm{S}$ characteristic function, we expect to obtain good similarity measurement. The KLD between two neighbor textured segments is given by [26]

$$KLD(s_1, s_2) = \frac{1}{18}\sum_{i=1}^{18}\left(\ln\left(\frac{c_1^i}{c_2^i}\right) - \frac{1}{\alpha_1^i} + \frac{2\gamma_2^i\Gamma\left(\frac{\alpha_2^i+1}{\alpha_1^i}\right)}{c_1^i\alpha_1^i\gamma_1^{(\alpha_2^i+1)/\alpha_1^i}}\right) \quad (8)$$

with

$$c_k = \frac{2\Gamma\left(\frac{1}{\alpha_k}\right)}{\alpha_k\gamma_k^{1/\alpha_k}} \quad k = 1, 2 \quad (9)$$

where $\Gamma(\cdot)$ is the Gamma function, s_1 and s_2 are the adjoining textured segments, and i denotes the index of the wavelet subband. The pair of regions with the minimum distance is merged until a maximum threshold of the distance is reached. In our experiments, a suggested value for the threshold is 0.4 for natural images and 0.6 for multimodal images. Compared to the previous work [19] in which the segments are classed into three categories, our two-category method offers comparable results with reduction in computational cost. Fig. 5(b) and (c) shows the merging results after few iterations of the region merging algorithm using KLD and Euclidean distance, respectively. Both images contain the same number of segmented regions. In addition, Fig. 5(d) and (e) shows the final segmentation at the end of the region merging process obtained using KLD and Euclidean distance, respectively. Clearly, the KLD provides better results than Euclidean distance in terms of human visual perception.

III. Region-Based Fusion Scheme

In this section, we introduce a new region-based image fusion scheme combining the wavelet decomposition and the $\mathrm{B}\alpha\mathrm{S}$ model with the feature fusion process by incorporating

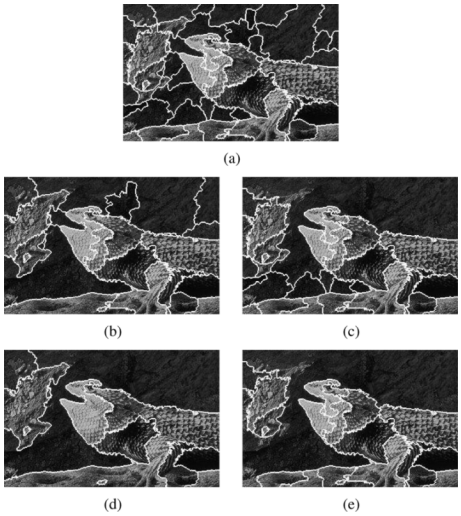

Fig. 5. Region merging results. (a) Result of the multiscale segmentation step. (b) Region merging using KLD. (c) Region merging using Euclidean distance. (d) Final merging result using KLD. (e) Final merging result using Euclidean distance.

the local information from the segmentation results obtained in Section II. For most image fusion applications, it seems more meaningful to combine semantic objects rather than pixels. As an intermediate step from a pixel-based scheme toward a semantic-based scheme, one may consider region-based approaches. There are a number of perceived advantages of combining a region-level fusion strategy with statistical techniques, including the following.

- **Reliable Fusion Rule:** Recent psychological experiments on human texture perception suggest that a good statistical model can approximate the marginal density of wavelet subband coefficients in a way that correlates well with the human visual perception [27].
- **Optimum Fusion Results:** Given the coefficients from each transformed image, feature extraction based on an appropriate statistical model can be achieved by means of optimum selection criteria.

A. Bivariate Alpha-Stable Distributions

Much like univariate stable distributions addressed in Section II, bivariate alpha-stable distributions are characterized by the stability property and the generalized central limit theorem [17]. However, unlike univariate stable distributions, bivariate alpha-stable distributions form a nonparametric set being thus much more difficult to describe. An exception is the family of multidimensional isotropic stable distributions whose characteristic function has the form

$$\varphi(\omega_1,\omega_2)=\exp(j(\delta_1\omega_1+\delta_2\omega_2)-\gamma|\boldsymbol{\omega}|^{\alpha}) \qquad (10)$$

where $\boldsymbol{\omega}=(\omega_1,\omega_2)$, and $|\boldsymbol{\omega}|=\sqrt{\omega_1^2+\omega_2^2}$. The distribution is isotropic with respect to the location point (δ_1,δ_2). The two marginal distributions of the isotropic stable distribution are $\mathrm{S}\alpha\mathrm{S}$ with parameters (δ_1,γ,α) and (δ_2,γ,α). As before, we will assume that the location $(\delta_1,\delta_2)=(0,0)$, while the parameters α and γ are used to measure the salient information contained within the regions in the image fusion process.

As in the case of the univariate $\mathrm{S}\alpha\mathrm{S}$ density function, when $\alpha\neq 1$ and $\alpha\neq 2$, no closed form expressions exist for the density function of bivariate alpha-stable random variables. A numerical algorithm for computing $\mathrm{B}\alpha\mathrm{S}$ densities has been developed by Nolan [28].

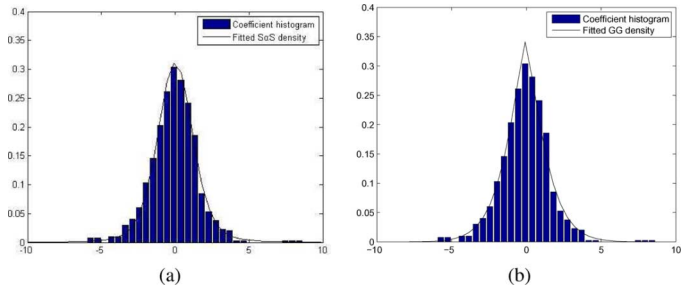

Fig. 6. (a) Region wavelet subband coefficients histogram fitted with a symmetric alpha-stable density. The estimated parameters are: $\alpha=1.6728$ and $\gamma=0.9140$, the KLD is: 0.012. (b) Region wavelet subband coefficients histogram fitted with a generalized Gaussian density. The estimated parameters are: $\alpha=1.5834$ and $\beta=1.2918$, the KLD is: 0.024.

B. Statistical Modeling Using $\mathrm{B}\alpha\mathrm{S}$ Distributions

Recent research in [29]–[31] showed that there are significant dependencies between wavelet coefficients. Bivariate models make it possible to exploit the inter-scale dependencies of wavelet decomposition. As addressed in [32], the authors described a statistical technique for removing noise from digital images by using bivariate alpha-stable distributions, which yielded superior results in terms of noise mitigation performance as well as in preserving fine signal details. In this work, we apply the $\mathrm{B}\alpha\mathrm{S}$ model to characterize the properties within the regions as well as the interdependencies across wavelet subbands. In the framework of wavelet analysis, we consider the isotropic case for $\mathrm{B}\alpha\mathrm{S}$ densities that is computationally feasible [33]. Therefore, the region characteristics are described via $\mathrm{B}\alpha\mathrm{S}$ densities by adaptively estimating the two parameters α and γ. Here we assume a constant γ in adjacent scales. Thus the estimation method addressed in [22], which is employed to univariate alpha-stable distributions, can be used in the isotropic bivariate cases by considering all the inter-scale coefficients as the same data Z, formed as

$$Z=[w_{l,\theta}(x,y),w_{l+1,\theta}(x,y)] \quad (x,y)\in r \qquad (11)$$

where r refers to the region, $w_{l,\theta}(x,y)$ is the detail coefficient in the l^{th} decomposition level and θ^{th} orientation band at location (x,y), and $w_{l+1,\theta}(x,y)$ is the parent coefficient at the coarser level corresponding to the same location in the image. Compared with the generalized Gaussian model proposed in [21], in which the two parameters defining the distribution are estimated using the second and fourth order moments of the data [34], our $\mathrm{B}\alpha\mathrm{S}$ model is more reliable to characterize the uniform features in a region which results in the second and fourth moments being equal to zero. In this special case, the generalized Gaussian model is no longer valid to estimate the region features as both its parameters equal to zero. $\mathrm{B}\alpha\mathrm{S}$ distributions provide a more accurate and desirable statistical model than generalized Gaussian densities.

Fig. 6(a) shows a typical example of a histogram of detail coefficients in a particular subband within a region, together with a plot of the fitted estimated univariate $\mathrm{S}\alpha\mathrm{S}$ model in comparison with the fitted GGD model using the moment estimator [34] in Fig. 6(b). As can be seen from the figure, the $\mathrm{S}\alpha\mathrm{S}$ provides

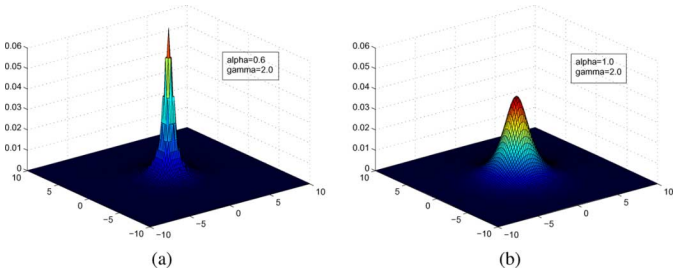

Fig. 7. (a) Graph of bivariate alpha-stable density corresponding to the values $\alpha = 0.6$ and $\gamma = 2.0$. (b) Graph of bivariate alpha-stable density corresponding to the values $\alpha = 1.0$ and $\gamma = 2.0$.

Fig. 8. (a) Match map: black regions correspond to similar area, and grey regions correspond to dissimilar area. (b) Decision map: light grey from the "UN Camp" IR image, dark grey from the "UN Camp" visible image, and black from similar region. (c) Weight map: light grey indicates majority contribution from the "UN Camp" visible image, dark grey indicates majority contribution from the "UN Camp" IR image, and black area is from dissimilar region.

a better fit than the GGD in terms of modeling the non-Gaussianity inherent in wavelet subbands. In addition, by incorporating the dependencies between parent and child coefficients across scales, the BαS model can also accurately describe the marginal behavior of wavelet coefficients in each region. As a result, with only two parameters defining the isotropic BαS distributions, we are able to represent the region characteristics. This results in a significant reduction in storage of the image region features, as well as in the computational complexity of the saliency and match measures.

C. Saliency and Match Measures

Saliency calculation, also expressed as activity or priority, is measuring to what degree is each coefficient from multimodal images salient in order to be chosen in the fused image. The meaning of "saliency" depends on the nature of the source images as well as on the particular fusion application. In [4], a simple activity measure taking the absolute value of the wavelet coefficient is used, which is given by

$$S(r) = \frac{1}{|r|} \sum_{(x,y)\in r} |w_{l,\theta}(x,y)| \tag{12}$$

where r denotes the region with size $|r|$, $w_{l,\theta}(x,y)$ is the detail coefficient at the lth decomposition level and θth orientation subband at location (x,y).

In the previous stage, each region in a particular subband is represented by two parameters α and γ from a BαS model. Examples of isotropic BαS density functions [33] for two different values of the characteristic exponent α are shown in Fig. 7. As it can be observed, the smaller α is, the more impulsive the corresponding BαS density is. This implies that the wavelet coefficients modeled by smaller characteristic exponent contain more structured information. Hence, we define the saliency measure for each decomposition level using both parameters α and γ as follows:

$$S^l(r) = \frac{1}{6}\sum_{\theta=1}^{6} \frac{\gamma_{l,\theta}(r)}{\alpha_{l,\theta}(r)} \qquad l = 1,2,3 \quad \theta = 1,2,\ldots,6 \tag{13}$$

where r refers to the region. l is the wavelet decomposition level, and θ is defined as the index of orientation band.

In Section II, we developed a region merging method by applying KLD as similarity metric between two adjacent segments across all the subbands. In probability theory, the Kullback–Leibler distance is a natural measurement from the data, referred to as the "true" probability distribution, to a model, a description or an approximation of the data. Therefore, we can use KLD as a statistical measure of similarity between the transform coefficients of the source images. The advantage of this scheme is that the match measure can be computed entirely on the estimated model parameters, which are typically small in size, so that it is able to accelerate the fusion process. Hence, the KLD defined in (8), which is applied to the univariate SαS densities, is also suitable to calculate the similarity distance between two estimated BαS models with two parameters (α,γ) at each decomposition level. Fig. 8(a) shows the match map obtained from the UNcamp infrared (IR) image and the UNcamp visible image. It can be seen that the salient objects from both images are classified as a dissimilar area while the backgrounds belong to a similar area.

Thus, in regions where the source images are distinctly different, it is appropriate to assume that only one of the source images provides most of the salient information while in regions where they are similar, a weighted combination may appear a better option. Here, we use the region entropy as a weighting factor. The normalized Shannon entropy of a region at each decomposition level is

$$P^l(r) = \frac{1}{6|r|}\sum_{\theta=1}^{6}\sum_{(x,y)\in r} w^2_{l,\theta}(x,y)\log w^2_{l,\theta}(x,y) \tag{14}$$

where r is the region with size $|r|$. The region size, shape or position could also be used to contribute to the weighting system. For the simple case where there are two input sources, we can express the decision process as

$$w_F^l(r) = \begin{cases} w_A^l(r), & \text{if } M_{AB}^l(r)>T \text{ and } S_A^l(r)>S_B^l(r) \\ w_B^l(r), & \text{if } M_{AB}^l(r)>T \text{ and } S_A^l(r)<S_B^l(r) \\ \mu_A^l w_A^l(r)+\mu_B^l w_B^l(r), & \text{otherwise} \end{cases} \tag{15}$$

where $M_{AB}^l(r)$ is the match metric computed by KLD in the region r at the lth decomposition level, $S_A^l(r)$ and $S_B^l(r)$ are the saliency measure defined in (13), $w_A^l(r)$ and $w_B^l(r)$ are the wavelet coefficients from source image A and source image B, respectively, $w_F^l(r)$ are the composite coefficients, and T is a threshold. It has been found experimentally that the best value of T is in the range of 0.005 to 0.02 for multisensor images. The weights μ_A^l and μ_B^l are obtained by

$$\mu_A^l(r) = \frac{P_A^l(r)}{P_A^l(r)+P_B^l(r)} \qquad \mu_B^l(r) = 1-\mu_A^l(r) \tag{16}$$

where $P_A^l(r)$ and $P_B^l(r)$ are the region entropy of source image A and source image B in the region r at the l^{th} decomposition level, respectively. The decision map produced by the above fusion rule is shown in Fig. 8(b). The algorithm always chooses

the region with the maximum activity value to determine which image each of the coefficients representing a region should come from, as both images have distinct features in the region. Fig. 8(c) shows the weight map which indicates how much salient information from each input image is incorporated into the fused result. On inspecting the figure, it is clear that the majority of the background from the visible image is more likely to play an important part in the fusion compared with the information contained in the IR image. This closely matches the human judgment.

D. Combination of Approximation Images

Because of their different physical meaning, the approximation and detail images are usually treated by the combination algorithm in different ways. A popular way to construct the fused approximation image L_F is

$$L_F = \frac{L_A + L_B}{2} \tag{17}$$

for example, the pixel- and region-level image fusion schemes proposed in [3] and [5]. However, equally weighing the input approximation images leads to the problem of contrast reduction in the case of opposite contrasts in different source images. In many approaches, the composite approximation coefficients of the highest decomposition level are taken to be a weighted average of the approximation of the sources. The logic behind this combination relies on the fact that statistical models are appropriate for modeling the detail coefficients, but not for the approximation image in the spatial domain. An alternative, presumptively better approach is a weighted combination method which maintains the actual means intensity of source images.

In this paper, we consider the region entropy as a way to measure the amount of salient information from the approximation images contributing to the fused result. Hence, the composite approximation image is generated by using the weighted combination

$$\begin{aligned} L_F(r) &= \nu_A(r)L_A(r) + \nu_B(r)L_B(r) \\ \nu_A(r) &= \frac{P_A(r)}{P_A(r) + P_B(r)} \qquad \nu_B(r) = 1 - \nu_A(r) \end{aligned} \tag{18}$$

where $P_A(r)$ and $P_B(r)$ are the region entropies of the source approximation images given in (14).

IV. Performance Assessment

In this section, we show experimental results obtained by means of subjective tests and objective performance measures for qualitatively and quantitatively assessing the performance of the proposed fusion methodology. In many applications, the human perception of the fused image is of paramount importance. Therefore, we choose different images, apply the algorithm, and visually evaluate the fused images in comparison with previously proposed pixel-level and region-level fusion schemes. The maximum selection (MS) scheme is a widely used combination method which considers the maximum absolute value of the wavelet coefficients from input images as the fused coefficients. It works well under the assumption that at each image location, only one of the source images provides the most useful information, but this assumption is not always valid. Another pixel-level fusion approach used for comparison was presented in [3] by making use of fractional lower order moments (FLOM) for SαS densities. A region-based image fusion scheme [5], referred to as RBCWT, is also used as a reference method. For both approaches we have used the authors' original implementations. For the sake of fair comparison, we use the parameters that were reported by the authors to yield the best fusion results. In addition, we also employ the proposed framework in order to implement two methods in which the BαS model is replaced with generalized Gaussian and univariate SαS densities, respectively. By doing so, we are able to study the effect of using different statistical models on the overall performance of the proposed methodology.

The first example in Fig. 9 shows fusion results for IR and visible images from the "UN Camp" sequence. In addition, the separate image region maps and joint region map are shown in Fig. 9(c)-(e). It can be observed that salient objects such as the human figure in the IR image and the roof of the building in the visible image are segmented into meaningful regions. Compared with the pixel-level method using the MS scheme shown in Fig. 9(i) and the FLOM fusion rule [3] shown in Fig. 9(h), the region-based methods produce images with better contrast that more accurately reflects the contrast of the original images. The figure also shows that the statistical algorithms [Fig. 9(f), (j), and (k)] are better at reducing blocking artefacts from the source images, which obviously appear around the human figure in the RBCWT method [Fig. 9(g)]. Each of these statistical models has successfully selected the majority of the background of the fused image from the visible image, while including the important features contained in the IR image.

As the second example, we illustrate the fusion of two input images depicting some people by the sea, with a kayak at sea. The results of these experiments are shown in Fig. 10. The "Kayak" IR and visible images have a strong contrast between their backgrounds, which is illustrative for assessing the saliency and match measures performance in selecting the correct regions during the fusion process. The figure demonstrates that all three statistical models select the majority of the background of the composite result, such as the sky and the sea, from the visible image, while the salient objects in the scene, such as the people, are selected from the IR image. Fig. 10(d)-(g) has some errors around the coastline and the human figures due to misregistration of the source images, which are not visible in the results obtained using the BαS and SαS models. There is no perceivable difference between the BαS and SαS models in this example. On inspecting Fig. 10, it can be seen that the GGD, BαS and SαS models do not accurately separate the sky and the sea. This is due to the fact that in the process of fusing the approximation subbands, higher weights are assigned to the background corresponding to the visible image. However, our main aim is to accurately to detect the salient objects "kayak" and human figures.

The last example shows the fusion of the "Tropical" IR and visible images which depict a human being hiding in a complex background. In comparison with pixel-based methods [Fig. 11(e) and (f)], we can clearly see that the region-based approaches preserve better the texture features from both the IR and visible images while reducing the sensitivity to noise and blurring effects. In this example, the advantages of using one statistical model over the other become apparent. Fig. 11(c) shows a better quality image than the results using the other two models due to the fact that BαS distributions more accurately model the region feature properties than the GGD and SαS distributions. Specifically, the BαS density not only models accurately the heavy-tailed behavior of the subband marginal distribution but it also captures the strong interdependencies

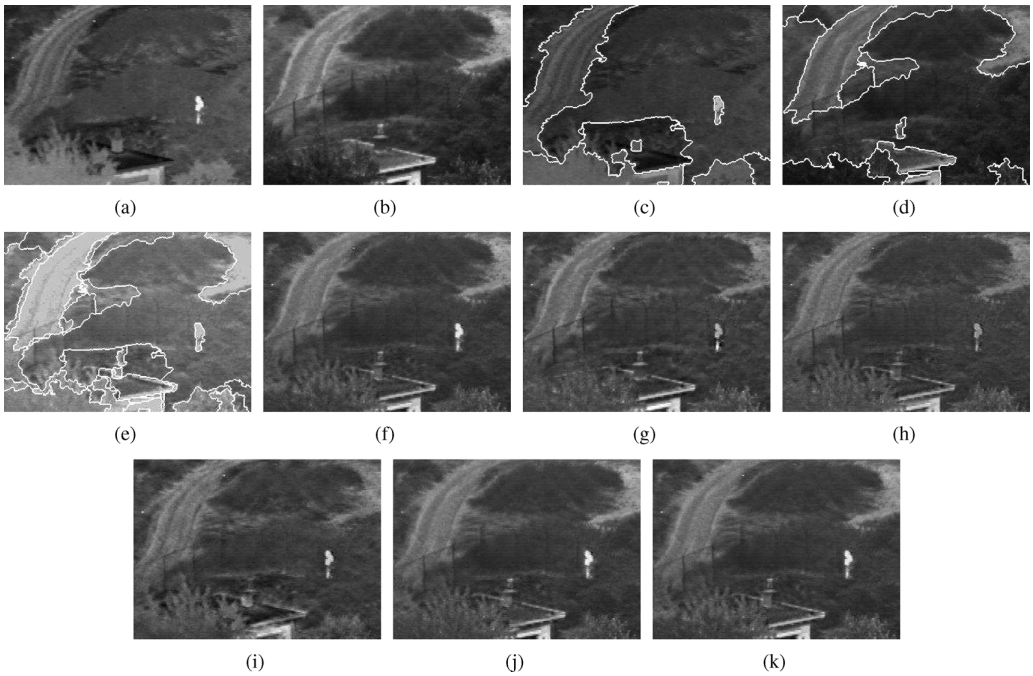

Fig. 9. Fusion of the "UN Camp" sequence. (a) Original IR image. (b) Original visible image. (c) IR image region map. (d) Visible image region map. (e) Joint region map. (f) Image fusion using $\mathrm{B}\alpha\mathrm{S}$ model. (g) Image fusion using RBCWT [5]. (h) Image fusion using FLOM rule [3]. (i) Image fusion using MS scheme. (j) Image fusion using GGD model. (k) Image fusion using $\mathrm{S}\alpha\mathrm{S}$ model.

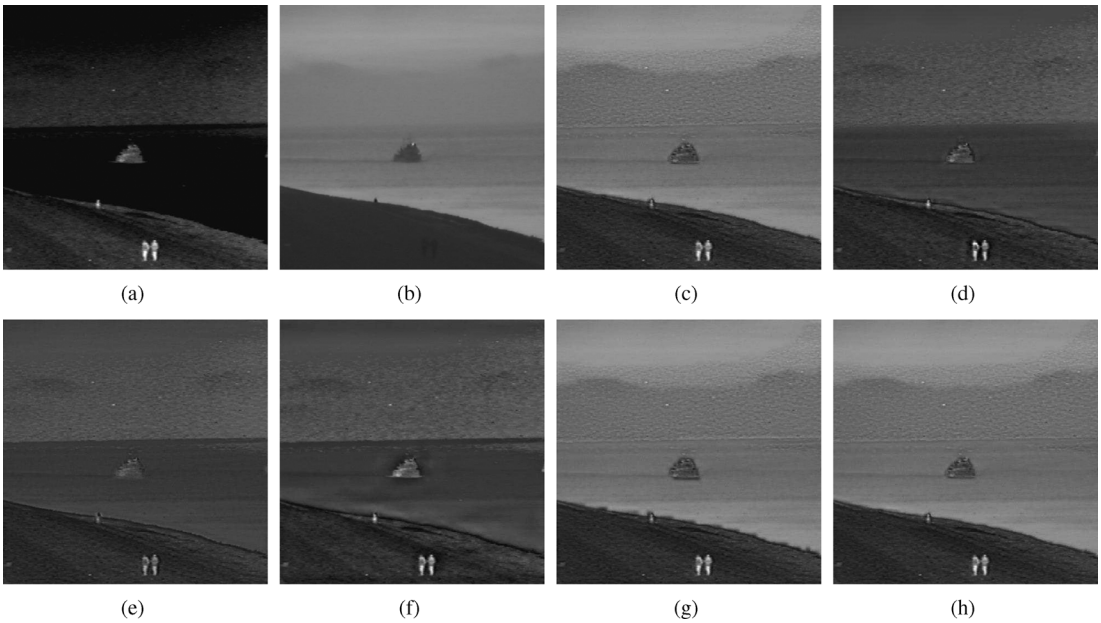

Fig. 10. Fusion of "Kayak" IR and visible images. (a) Original IR image. (b) Original visible image. (c) Image fusion using $\mathrm{B}\alpha\mathrm{S}$ model. (d) Image fusion using RBCWT [5]. (e) Image fusion using FLOM rule [3]. (f) Image fusion using MS scheme. (g) Image fusion using GGD model. (h) Image fusion using $\mathrm{S}\alpha\mathrm{S}$ model.

between wavelet coefficients at different scales. For instance, a coefficient with a high value appearing in the current scale which does not have a correspondingly high coefficient appearing in the lower adjacent scale is probably caused by noise.

Although in the literature the majority of image fusion performance tests tend to be subjective, e.g., based on psycho-visual studies, the main disadvantage of this approach is that it is time consuming and requires often expensive experiments with human subjects. Objective fusion evaluation can also be performed to compare results obtained using different algorithms. A quality assessment metric which does not require a ground-truth was proposed by Piella and Heijmans [35] based on an image quality metric introduced in [36]. In their approach, the important edge information of human visual system is taken into account to evaluate the relative amount of salient information contained in each of the input images that has been transferred into the fused image without introducing distortions. Petrovic and Xydeas proposed a metric [37], which measures the edge information using a Sobel edge detector as well as the orientation information at each pixel in both source and the fused images. In this paper, we use their defined criteria to evaluate the fusion performance. The results using Piella metric are shown in Table I,

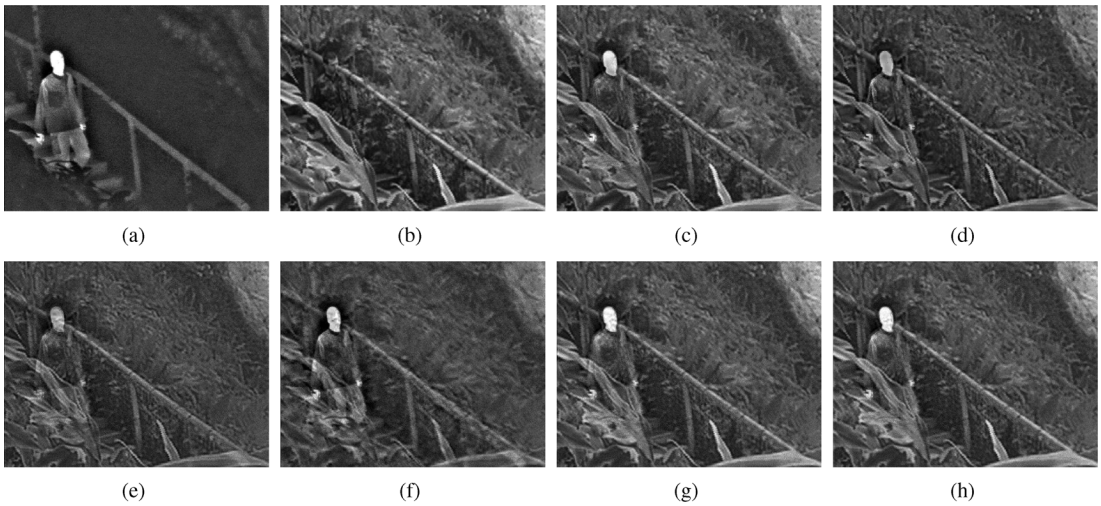

Fig. 11. Fusion of "Tropical" IR and visible images. (a) Original IR image. (b) Original visible image. (c) Image fusion using $\mathrm{B}\alpha\mathrm{S}$ model. (d) Image fusion using RBCWT [5]. (e) Image fusion using FLOM rule [3]. (f) Image fusion using MS scheme. (g) Image fusion using GGD model. (h) Image fusion using $\mathrm{S}\alpha\mathrm{S}$ model.

TABLE I
PERFORMANCE COMPARISONS USING PIELLA'S METRIC Q_w [35]

Example	Methods					
	MS	RBCWT [5]	FLOM [3]	GGD	SαS	**BαS**
UN Camp IR and Visible	0.5869	0.6829	0.6861	0.6983	0.7071	**0.7087**
Kayak IR and Visible	**0.7482**	0.7051	0.7113	0.7206	0.7207	0.7238
Tropical IR and Visible	0.5735	0.7676	0.7319	0.7651	0.7756	**0.7824**
medical MRI and CT	0.5976	0.6722	0.5274	0.7497	0.7518	**0.7541**

TABLE II
PERFORMANCE COMPARISONS USING PETROVIC'S METRIC $Q^{AB/F}$ [37]

Example	Methods					
	MS	RBCWT [5]	FLOM [3]	GGD	SαS	**BαS**
UN Camp IR and Visible	0.4054	0.5069	0.4578	0.4993	0.4572	**0.5106**
Kayak IR and Visible	**0.7472**	0.7368	0.7133	0.7204	0.7361	0.7395
Tropical IR and Visible	0.3093	**0.5054**	0.4175	0.4331	0.4561	0.5018
medical MRI and CT	0.5576	0.6339	0.4684	0.6324	0.6682	**0.6808**

which indicate that the three statistical fusion algorithms obtain the higher evaluation values compared with the previously proposed pixel and region-level approaches, except for the "Kayak" images when the MS scheme is rated highest. Table II shows the Petrovic metric results. Both metrics show that employing the $\mathrm{B}\alpha\mathrm{S}$ model leads to the best results among all three statistical models. In fact, due to the actual definitions of these metrics, a difference of 0.01 is significant for the quality improvement. We have found that Piella and Petrovic metrics generally correlate well with the results of visual analysis. However, it should be noted that these metrics are based on edges and consequently, fused images containing significant artefacts such as ringing introduced by the transform can sometimes be inadvertently rated high by the metrics but look inferior perceptually.

In terms of computational complexity, our proposed method is more expensive than the RBCWT due to the additional model parameter estimation component. Also, compared with FLOM, it includes the extra image segmentation step whereas FLOM is a pixel-level approach. The running time for our method which uses un-optimised Matlab code is around 17 s on Intel Pentium 4 3.00-GHz machines to fuse two 256×256 test images whereas the average CPU time taken by RBCWT is about 10 s. FLOM needs approximately 2 s in the same conditions.

V. CONCLUSIONS AND FUTURE WORK

In this paper, we introduced a novel region-based image fusion framework that integrates multiscale image segmentation and a statistical fusion scheme. In the segmentation component of our methodology, the local statistical characteristics of images have been employed in order to drive the initial texture segmentation process. In the fusion component, the salient information contained in the regions was modeled using bivariate alpha-stable distributions. These have the advantage of also capturing the dependencies of wavelet coefficients across scales. As a match measure the Kullback–Leibler distance between $\mathrm{B}\alpha\mathrm{S}$ models was proposed. A number of advantages of this fusion scheme over previously proposed pixel-based and region-based methods have been discussed. Experimental results confirm the superiority of the region based image fusion method based on the $\mathrm{B}\alpha\mathrm{S}$ model over previously proposed pixel- and region-level fusion approaches. Future work will concentrate on the development of higher-complexity region based fusion rules that will incorporate the inter-scale and inter-orientation dependencies into the decision and combination processes. In addition, an interesting direction for future work could be the extension of the proposed fusion scheme to the case of multiple input images.

ACKNOWLEDGMENT

The authors would like to thank N. Kingsbury for his assistance in providing the code for the DT-CWT. The original "UN Camp" and "Kayak" IR and visible images were kindly supplied by A. Toet of the TNO Human Factors Research Institute. All images including medical MRI and CT images are available online at http://www.imagefusion.org.

REFERENCES

[1] M. Abidi and R. Gonzalez, *Data Fusion in Robotics and Machine Intelligence*. New York: Academic, 1992.

[2] H. Li, B. S. Manjunath, and S. K. Mitra, "Multisensor image fusion using the wavelet transform," *Graph. Models Image Process.*, vol. 57, no. 3, pp. 235–245, May 1995.
[3] A. M. Achim, C. N. Canagarajah, and D. R. Bull, "Complex wavelet domain image fusion based on fractional lower order moments," in *Proc. Int. Conf. Information Fusion*, Jul. 2005, vol. 1, pp. 515–521.
[4] G. Piella, "A general framework for multiresolution image fusion: From pixels to regions," *Inf. Fus.*, vol. 4, pp. 259–280, Apr. 2003.
[5] J. J. Lewis, R. J. O'Callaghan, S. G. Nikolov, D. R. Bull, and N. Canagarajah, "Pixel- and region-based image fusion with complex wavelets," *Inf. Fus.*, vol. 8, no. 2, pp. 119–130, Apr. .
[6] R. J. O'Callaghan and D. R. Bull, "Combined morphological-spectral unsupervised image segmentation," *IEEE Trang. Image Process.*, vol. 14, no. 1, pp. 49–62, Jan. 2005.
[7] J. Yang and R. S. Blum, "A region-based image fusion method using the expectation-maximization algorithm," in *Proc. Conf. Information Sciences and Systems*, Mar. 2006, pp. 468–473.
[8] D. K. Panjwani and G. Healey, "Markov random field models for unsupervised segmentation of textured color images," *IEEE Trans. Pattern Anal. Machine Intell.*, vol. 17, no. 10, pp. 939–954, Oct. 1995.
[9] Y. Delignon, A. Marzouki, and W. Pieczynski, "Estimation of generalized mixtures and its application in image segmentation," *IEEE Trans. Image Process.*, vol. 6, no. 10, pp. 1364–1375, Oct. 1997.
[10] J.-P. Wang, "Stochastic relaxation on partitions with connected components and its application to image segmentation," *IEEE Trans. Pattern Anal. Machine Intell.*, vol. 20, no. 6, pp. 619–636, Jun. 1998.
[11] Y. Deng and B. S. Manjunath, "Unsupervised segmentation of color-texture regions in images and video," *IEEE Trans. Pattern Anal. Machine Intell.*, vol. 23, no. 8, pp. 800–810, Aug. 2001.
[12] J. Shi and J. Malik, "Normalized cuts and image segmentation," *IEEE Trans. Pattern Anal. Machine Intell.*, vol. 22, no. 8, pp. 888–905, Aug. 2000.
[13] J. Chen and T. N. Pappas, "Adaptive perceptual color-texture image segmentation," *IEEE Trans. Image Process.*, vol. 14, no. 10, pp. 1524–1536, Oct. 2005.
[14] A. Achim, A. Bezerianos, and P. Tsakalides, "Novel Bayesian multiscale method for speckle removal in medical ultrasound images," *IEEE Trans. Med. Imag.*, vol. 20, no. 8, pp. 772–783, Aug. 2001.
[15] A. Achim, P. Tsakalides, and A. Bezerianos, "SAR image denoising via Bayesian wavelet shrinkage based on heavy-tailed modeling," *IEEE Trans. Geosci. Remote Sens.*, vol. 41, no. 8, pp. 1773–1784, Aug. 2003.
[16] G. Samorodnitsky and M. S. Taqqu, *Stable Non-Gaussian Random Processes: Stochastic Models with Infinite Variance*. New York: Chapman & Hall, 1994.
[17] C. L. Nikias and M. Shao, *Signal Processing with Alpha-Stable Distributions and Applications*. New York: Wiley, 1995.
[18] N. Kingsbury, "Complex wavelets for shift invariant analysis and filtering of signals," *Appl. Computt. Harmon. Anal.*, vol. 10, pp. 234–253, May 2001.
[19] T. Wan, N. Canagarajah, and A. Achim, "Multiscale color-texture image segmentation with adaptive region merging," in *Proc. IEEE Conf. Acoustics, Speech, and Signal Processing*, Honolulu, HI, Apr. 2007, pp. 1213–1216.
[20] T. Wan, N. Canagarajah, and A. Achim, "Statistical multiscale image segmentation via alpha-stable modeling," in *Proc. IEEE Conf. Image Processing*, San Antonio, TX, Sep. 2007, pp. 357–360.
[21] T. Wan, N. Canagarajah, and A. Achim, "Region-based multisensor image fusion using generalized Gaussian distribution," in *Proc. Int. Workshop Nonlinear Signal and Image Processing*, Sep. 2007.
[22] X. Ma and C. L. Nikias, "Parameter estimation and blind channel identification in impulsive signal environment," *IEEE Trans. Signal Process.*, vol. 43, no. 12, pp. 2884–2897, Dec. 1995.
[23] R. C. Gonzalez and R. E. Woods, *Digital Image Processing*, 2nd ed. Englewood Cliffs, NJ: Prentice-Hall, 2002.
[24] Y. Deng, C. Kenney, M. S. Moore, and B. S. Manjunath, "Peer group filtering and perceptual color image quantization," in *Proc. IEEE Int. Symp. Circuits and Systems VLSI*, Jun. 1999, vol. 4, pp. 21–24.
[25] A. Gersho and R. M. Gray, *Vector Quantization and Signal Compression*. Norwell, MA: Kluwer, 1993.
[26] G. Tzagkarakis and P. Tsakalides, "A statistical approach to texture image retrieval via alpha-stable modeling of wavelet decompositions," in *Proc. 5th Int. Workshop Image Analysis for Multimedia Interactive Services*, Apr. 2004.
[27] J. R. Bergen, "Theories of visual texture perception," in *Vision and Visual Dysfunction*, D. Regan, Ed. Macmillan: New York, 1991, vol. 10.
[28] J. P. Nolan, *Multivariate Stable Distributions: Approximation, Estimation, Simulation and Identification*, R. J. Adler, R. E. Feldman, and M. S. Taqqu, Eds. Boston, MA: Birkhauser, 1998, A Practical Guide to Heavy Tails.
[29] S. Mallat and S. Zhong, "Characterization of signals from multiscale edges," *IEEE Trans. Pattern Anal. Machine Intell.*, vol. 14, no. 7, pp. 710–732, Jul. 1992.
[30] M. N. Do and M. Vetterli, "Rotation invariant texture characterization and retrieval using steerable wavelet-domain hidden Markov models," *IEEE Trans. Multimedia*, vol. 4, no. 4, pp. 517–527, Dec. 2002.
[31] M. Crouse, R. D. Nowak, and R. G. Baraniuk, "Wavelet-based signal processing using hidden Markov models," *IEEE Trans. Signal Process,* Special Issue on Wavelet and Filterbanks, vol. 46, no. 4, pp. 886–902, Apr. 1998.
[32] A. Achim and E. E. Kuruoglu, "Image denoising using bivariate α-stable distributions in the complex wavelet domain," *IEEE Signal Process. Lett.*, vol. 12, no. 1, pp. 17–20, Jan. 2005.
[33] J. P. Nolan, "Multivariate stable densities and distribution functions: General and elliptical case," in *Proc. Deutsche Bundesbank's 2005 Annu. Fall Conf.*, Nov. 2005.
[34] E. P. Simoncelli and E. H. Anderson, "Noise removal via Bayesian wavelet coring," in *Proc. IEEE Int. Conf. Image Processing*, Sep. 1996, vol. 1, pp. 379–382.
[35] G. Piella and H. Heijmans, "A new quality metric for image fusion," in *Proc. IEEE Int. Conf. Image Processing*, Sep. 2003, vol. 2, pp. 173–176.
[36] Z. Wang and A. Bovik, "A universal image quality index," *IEEE Signal Process. Lett.*, vol. 9, no. 3, pp. 81–84, Mar. 2002.
[37] V. Petrovic and C. Xydeas, "On the effects of sensor noise in pixel-level image fusion performance," in *Proc. Int. Conf. Image Fusion*, Jul. 2000, vol. 2, pp. 14–19.

Tao Wan (S'07) received the B.Eng. degree (Hons) in computer science from the University of Science and Technology, Beijing, China in 2000 and M.S. degree in multimedia and computing from the University of Bristol, Bristol, U.K., in 2004. Currently, she is pursuing the Ph.D. degree in the Image Communications Group, Centre for Communications Research, University of Bristol.

Her research interests include signal processing, image segmentation, statistical modeling, contend-based image analysis, and image fusion.

Nishan Canagarajah (M'95) received the B.A. (Hons.) and Ph.D. degrees in DSP techniques for speech enhancement, both from the University of Cambridge, Cambridge, U.K.

He is currently a Professor of multimedia signal processing at the University of Bristol, Bristol, U.K. He was previously a Research Assistant and Lecturer at Bristol, investigating DSP aspects of mobile radio receivers. His research interests include image and video retrieval as well as 3-D video and image fusion. He is widely supported in these areas by industry, the EU, and the EPSRC. He has published more than 160 papers and two books.

Prof. Canagarajah is a member of the EPSRC Peer Review College.

Alin Achim (S'99–M'04–SM'09) is a Lecturer in signal processing with the Department of Electrical and Electronic Engineering at the University of Bristol, Bristol, U.K. His research interests are in statistical image and video processing and multiresolution algorithms with applications in remote sensing and medical imaging. For additional biographical information, visit http://www.bristol.ac.uk/eeng/department/staff/aa-personal.